Effect of different good solvents in flash nano-precipitation via multi-scale population balance modeling-CFD coupling approach

Effect of Different Good Solvents in Flash Nano-Precipitation via Multi-scale Population Balance Modeling-CFD coupling approach

Alessio D. Lavino[1], Marco Ferrari*, Antonello A. Barresi, Daniele Marchisio

Department of Applied Science and Technology, Institute of Chemical Engineering, Politecnico di Torino, 10129 Torino, Italy

Abstract

A computational and modeling approach is used to highlight the key factors that affect the polymer nanoparticles (NP) size in flash nano-precipitation (FNP), when the good solvent, e.g., acetone, is replaced by acetonitrile, tetrahydrofuran and tert-butanol. A population balance model is coupled with computational fluid dynamics to study the kinetics effects on FNP. The mean NP size is predicted in terms of mean radius of gyration via the Flory law of real polymers. The effect of different good solvents is modeled in terms of solute-solvent interactions, using the Flory-Huggins theory and Hansen solubility parameters. Promising results show how the proposed methodology is

Abbreviations: ACT, acetone; ACN, acetonitrile; CMD, cluster mass distribution; CFD, computational fluid dynamics; CIJM, confined impinging jets mixer; DQMOM-IEM, direct quadrature method of moments coupled with the interaction and exchange with the mean; FNP, flash nano-precipitation; HSP, Hansen solubility parameters; NP, Nanoparticles; PCL, poly-ε-caprolactone; PBM, population balance model; PDF, probability density function; QMOM, quadrature method of moments; TBA, tert-butanol; THF, tetrahydrofuran.

*Corresponding author

Email address: marco.ferrari@polito.it (Marco Ferrari)

[1]Present address: Department of Chemical Engineering, Imperial College London, South Kensington Campus, London SW7 2AZ, UK

able to investigate the role played by different good solvents, analyzing single factors at the time. A deep insight into both the dynamics of mixing and the dynamics of aggregation is therefore reached and the main mechanisms involved are pointed out, showing a good agreement with experimental data.

Keywords: Flash Nano-Precipitation, Hansen Solubility Parameters, Flory-Huggins Theory, Population Balance Model, CFD

1. Introduction

Nanoparticles (NP) production has been widely investigated in the last decade, due to the wide range of its applications such as cosmetics, pharmaceuticals, textiles, agriculture, and food science (Das et al., 2009; Demetzos, 2016; Nelson, 2002; Prasad et al., 2014; Wu and Guy, 2009). The control of the final NP size and particle size distribution is of paramount importance, especially in controlled drug delivery systems applications, in which a threshold dimension must not be exceeded to guarantee the correct drug release at the targeted area inside the blood stream (Hans and Lowman, 2002; Petitti et al., 2008). In particular, polymer NP formation received a lot of attention from both experimental and modeling approaches, in order to determine the key parameters that govern the final NP targeted size (Celasco et al., 2014; Valente et al., 2012a,b; Zelenková et al., 2018). Due to their biological applications, polymers must be biocompatible and non-toxic; here, poly-ε-caprolactone (PCL) is used, since it has been considered one of the best candidates for this purpose (Who et al., 2000). One of the most used techniques for NP production is represented by the so-called flash nano-precipitation (FNP). It consists in the mixing of a 'good solvent' in which the

polymer is dissolved and a 'bad solvent' (also named as anti- or non-solvent), which is miscible with the good solvent but not compatible with the polymer. The anti-solvent destabilizes the mixture inducing polymer aggregation and precipitation of the formed NP. The phenomenon that governs NP formation just described above is also labelled as solvent displacement (Saad and Prud'homme, 2016).

Several studies have been already carried out to understand fluid dynamics effects at macro- and micro-scales (Johnson and Prud'homme, 2003b; Liu and Fox, 2006) for the confined impinging jets mixer (Johnson and Prud'homme, 2003a) (CIJM) and also for different geometries, such as the vortex mixer (VM) (Marchisio et al., 2009, 2008), the multi-inlet vortex mixer (MIVM) (Liu et al., 2008), the T-mixer (Gradl et al., 2006) and the Y-mixer (Choi et al., 2005). Other experimental (Lince et al., 2008) and modeling (Cheng et al., 2010; Di Pasquale et al., 2012; Lavino et al., 2015, 2017) attempts also showed the importance of accounting for the kinetics besides the thermodynamics for FNP. However, numerous are still the open topics under debate that need to be addressed. One of them is represented by the effect of different good solvents in NP formation via FNP and has become a crucial aspect of the industrial NP production. Here, the interesting case of NP formation in CIJM is considered, with PCL as solute and water as anti-solvent. Four different good solvents are investigated: acetone (ACT), acetonitrile (ACN), tetrahydrofuran (THF) and tert-butanol (TBA).

The experimental procedure for polymeric NP production through solvent displacement has been extensively applied throughout the years, testing different polymers; in particular, it was validated for PCL, obtaining also good

incorporation efficiency with different loading substances (Barresi et al., 2015; Celasco et al., 2014; Ferri et al., 2017; Lavino et al., 2019; Lince et al., 2008, 2009, 2011; Massella et al., 2018; Valente et al., 2012a,b; Zelenková et al., 2015, 2014). In experiments, water quenching (i.e. sudden dilution with distilled water) is employed as stabilization technique over time of the precipitated NP (Barresi et al., 2015; Ferri et al., 2017; Zelenková et al., 2015, 2014), preventing further aggregation in the reactor outlet (Barresi et al., 2015; Saad, 2007) and preserving the particle distribution. This is implicitly taken into account in our modeling approach by 'freezing' the predicted NP sizes at the outlet of the mixer (Lavino et al., 2017, 2019; Lince et al., 2009) allowing a consistent comparison with the experimental data, as it will be explained more clearly in the theoretical and modeling section of this work.

Experiments showed how different NP size and size distribution may be reached by just changing the good solvent (Ferri et al., 2017; Zelenková et al., 2015), a crucial aspect in several industrial contexts. At this level of description, from the experiments side, it is hard to fully understand the parameters that play a key role in determining different mean NP size at the outlet of the process. Hence, modeling and simulations are here employed to further examine those aspects and, eventually, to analyze them separately. A population balance model (PBM) which uses molecules as building blocks coupled with computational fluid dynamics (CFD) approach is used, already proposed and validated in an our previous work (Lavino et al., 2017), where the presence of the drug is neglected, as also in this present work. The main novelty of the proposed methodology consists in the incorporation of the thermodynamics theory of Flory-Huggins interaction parameter (Hansen, 2007) inside the ki-

netic model (PBM-CFD) to study the different good solvent effects on the final predicted NP size. Recent efforts also showed at the molecular scale the importance of accounting for the thermodynamics on the polymer conformation in mixtures (Gartner and Jayaraman, 2018; Lavino et al., 2018, 2020; Martin and Jayaraman, 2016). More specifically, the Flory-Huggins interaction parameter χ is here correlated to the mean radius of gyration, expressed, in turn, in terms of Flory law (Flory, 1953). The solubility of PCL is accounted for by using the Hansen solubility parameters (HSP) for the different solvents investigated in this work. This modeling approach brings the advantage of considering thermodynamic quantities inside the kinetic model, such as the Flory-Huggins χ parameter and the HSP, extensively reported in literature for a wide range of solvents and, more importantly, shows how to correlate them to the prediction of the final mean NP size. In this way, it is possible to readily obtain a transferable model, when different good solvents are used in FNP. Kinetics and thermodynamics are therefore intertwined in a unique modeling tool and used to investigate the effect of different good solvents on NP precipitation. Another very important advantage is the possibility to analyze single factors at a time, unlike experiments, getting a deeper insight into the main phenomena. In this way, the dynamics of mixing is studied separately from the dynamics of aggregation, highlighting the physical and modeling properties that mainly influence polymer aggregation, when different good solvents are used.

The paper is structured as follows: modeling and theoretical backgrounds are presented in section 2, with particular attention to the multi-scale kinetic model (CFD and population balance model) together with the thermodynam-

ics of NP formation by solvent displacement; then, operating conditions and numerical details are reported in section 3. The main results are discussed in section 4 and, finally, conclusions and future developments are presented in section 5.

2. Theoretical Background

This section is dedicated to the theoretical background and the modeling strategy adopted in this work. The theory presented here is divided into two main subsections: *i*. the kinetic model, in which the main equations of the population balance model (PBM) and computational fluid dynamics (CFD) are presented; *ii*. the thermodynamic model, used to study the solute-solvent interactions, with a particular focus on the theory of real polymers in solution.

The PBM-CFD coupling approach is able to describe the effect of kinetics on NP precipitation by accounting for the interplay of many factors, such as the inlet flow rate, the turbulent mixing and the particles-collision dynamics (details thereof will be presented in section 2.1), which have been proven to strongly affect the final NP size at certain operating conditions (Lavino et al., 2017). More specifically, the PBM predicts the mean particles size at the outlet of the mixer, as well as the evolution of the particles size distribution, also named cluster mass distribution (CMD), as it will be labelled from now on. On the other hand, the thermodynamics of real polymers is used to build up a modeling bridge, able to embrace the different good solvent effects, and strictly interconnected to the PBM, as it will be explained in section 2.2.

Regarding the flow field, the steady-state Favre-averaged continuity and

Navier–Stokes equations are solved in the CFD code, together with the equations for the turbulent kinetic energy, k, and the turbulent dissipation rate, ε, in line with the standard $k-\varepsilon$ turbulence model (Andersson et al., 2012). As these equations are very well known and already implemented in the CFD code, they are omitted here for a sake of brevity and the readers can refer to our previous work Di Pasquale et al. (2012) for further details. The Favre-average approach (Favre, 1965) is necessary, since two fluids with different densities are involved. The fluid can still be considered incompressible, but density fluctuations are taken into account in this way.

The effect of turbulent fluctuations on NP formation is modeled by the direct quadrature method of moments, coupled with the interaction-by-exchange-with-the-mean (DQMOM-IEM) method (Marchisio and Fox, 2005), in which two nodes/environments are employed for the quadrature procedure. Below, two subsections are dedicated respectively to the PBM (aggregation dynamics and micro-mixing models) and the thermodynamics of real polymers in solution, presenting the main modeling details employed in this work.

2.1. Population Balance Model for FNP

A population balance model (PBM) is employed to describe the evolution of the cluster mass distribution (CMD). Being this model extensively presented in our previous work, here we report only the definition of the CMD and the kinetic equation in which the moments of the CMD are transported. For a complete detailed description of the PBM, please refer to Lavino et al. (2017). The CMD is modeled with a number density function, $f(\mathbf{x}, n)$, defined in such a way that the quantity $f(\mathbf{x}, n)\mathrm{d}n$ represents the number density of NP, or molecular clusters, containing n macromolecules at position $\mathbf{x}$.

The term 'macromolecule' is here referred to as PCL molecule of molecular weight $M_W = 14000$ g mol^{-1}. The variable n is labelled as dimensionless cluster mass or aggregation number and it can be treated as a continuous variable, since it varies from one to very large numbers. In the pure good solvent stream the PCL is completely dissolved and no aggregation takes place. Therefore, the CMD corresponds to a Dirac delta function centred in $n = 1$. By normalising the CMD with the Avogadro number (necessary to keep the simulations numerically stable), the CMD in the good solvent stream (initial conditions) corresponds to the initial polymer molar concentration.

The PBM is here solved with the quadrature method of moments (QMOM) approach (Marchisio and Fox, 2013). Let us recall the definition of the generic j^{th}-order moment:

$$m^{(j)} = \int_0^\infty f(n) n^j \mathrm{d}n. \tag{1}$$

The advantage is twofold: on one hand, the computational cost is heavily reduced, compared to other discretized methods (Marchisio and Fox, 2013); on the other hand, the moments of the CMD represent physical measurable quantities. Indeed, $m^{(0)}$ is the total cluster number density, $m^{(1)}$ is a conserved quantity and corresponds to the total number density of macromolecules, whereas the ratio between $m^{(1)}$ and $m^{(0)}$ results in the average number of macromolecules per NP or molecular cluster.

By applying the moment transform and the Favre average $\langle \cdot \rangle$, the steady-state transport equation for the j^{th}-order moment of the CMD $f(n)$ reads as follows:

$$\frac{\partial}{\partial \mathbf{x}} \cdot \left(\bar{\rho}\langle \mathbf{U}\rangle \left\langle m^{(j)}\right\rangle\right) - \frac{\partial}{\partial \mathbf{x}} \cdot \left(\bar{\rho}\Gamma_t \frac{\partial \left\langle m^{(j)}\right\rangle}{\partial \mathbf{x}}\right) =$$

$$= \frac{\bar{\rho}}{2}\left\langle \int_0^\infty \int_0^\infty \left[(n+n')^j - n^j - n'^j\right] \beta(n,n') f(n) f(n') \mathrm{d}n \mathrm{d}n' \right\rangle, \quad (2)$$

where $\Gamma_t \approx \nu_t/0.7$, is the turbulent diffusivity which is much larger than the Brownian diffusivity and is calculated from the turbulent viscosity, ν_t, by assuming a turbulent Schmidt number of 0.7 (Andersson et al., 2012), $\bar{\rho}$ is the time-averaged fluid density and $\langle \mathbf{U}\rangle$ is the Favre-averaged fluid velocity, as the particle Stokes number is much less than unity (Baldyga and Orciuch, 2001). The aggregation kernel, $\beta(n,n')$, that appears in the source term on the right hand side of Eq. (2) represents the rate with which two clusters (or, equally, nanoparticles) collide and aggregate (second order point process Marchisio and Fox (2013)). The source term consists of two contributions: a negative term that states the disappearance of two clusters containing respectively n and n' polymer macromolecules, and the appearance of the aggregate cluster (positive term) formed by $n + n'$ macromolecules. It is noteworthy to stress that molecular dynamics investigations (Di Pasquale et al., 2014) have shown that the freely-jointed chain model (Rubinstein and Colby, 2003) can be applied in this mathematical formulation, so that a cluster made by n molecules of molecular weight M_w will behave as a cluster made by one single PCL molecule of molecular weight $n \cdot M_w$. This assumption affects the formula used for the mean clusters size, in terms of Flory law, as it will be shown in section 2.2.

The aggregation kernel accounts for two mechanisms: Brownian motions

and turbulent fluctuations. Here, the assumption is that these two contributions are simply additive, and it holds on the physical evidence that at low initial polymer concentration in good solvent stream, Brownian aggregation dominates over the turbulent one, and vice versa at high initial polymer concentration. Applying the Stokes-Einstein formulation (Elimelech et al., 1998), the aggregation kernel in function of the mean radius of gyration of the two NP, or molecular clusters, that are self-assembling or aggregating assumes the following expression (Cheng et al., 2010):

$$\beta(n,n') = \eta\frac{2k_BT}{3\mu}\frac{\left(\llbracket R_g(n,x_s)\rrbracket + \llbracket R_g(n',x_s)\rrbracket\right)^2}{\llbracket R_g(n,x_s)\rrbracket\llbracket R_g(n',x_s)\rrbracket} + \\ + 1.2944\eta\sqrt{\frac{\varepsilon}{\nu}}\left(\llbracket R_g(n,x_s)\rrbracket + \llbracket R_g(n',x_s)\rrbracket\right)^3, \quad (3)$$

where μ is the molecular viscosity of the suspending liquid (i.e. mixture of the good and bad solvents and therefore function of the good solvent molar fraction x_s (Lavino et al., 2017)), k_B is the Boltzmann constant, ε is the turbulent dissipation rate, ν is the mixture kinematic viscosity and $\llbracket\cdot\rrbracket$ represents the ensemble-average.

The term η stands for an aggregation efficiency, only dependent on the initial supersaturation ratio. It is represented by a stepwise function: zero for undersaturated solutions and one for supersaturated solutions. The supersaturation ratio is defined as the ratio between the local PCL concentration and its equilibrium one. Their expressions are reported in our previous work (Lavino et al., 2017). When the supersaturation ratio is locally greater than unity, or in other words when the local PCL concentration is greater than its

local solubility (i.e., equilibrium concentration), which in turn depends on the local solvent composition, self-assembly and aggregation are triggered; namely PCL molecular self-assemble forming NP that then further aggregate forming the final NP. The main assumption is that molecules are more stable when in a molecular cluster and therefore they self-assemble or aggregate irreversibly. This implies that the energy barrier for particle formation is null and therefore particle formation, under these conditions, can be interpreted as spinodal decomposition rather than nucleation. In line with the classical nucleation theory this model is applicable only when the initial supersaturation is very large, as also found out in our previous work, where the model was originally validated by Lavino et al. (2017). An accurate quantification of the precipitated PCL with respect to what is left in solution during FNP still remains an unsolved issue; when the supersaturation ratio is much larger than unity, it is reasonable to assume that most of PCL precipitates out with the operating conditions investigated in this work.

$[\![R_g(n, x_s)]\!]$ represents the ensemble-averaged radius of gyration, dependent on the aggregation number n and on the good solvent molar fraction x_s. It is expressed in terms of the Flory law, as explained in subsection 2.2.

Moreover, the dynamics of mixing is also considered, as turbulence fluctuations and local mixing gradients (supersaturation) affect PCL aggregation. More specifically, the solvent mixture fraction is described in terms of probability density function (PDF) for the good solvent mass fraction, ξ, in the good solvent-water mixture. As anticipated above in the text, mixing is treated with the DQMOM-IEM approach with only two nodes/environments. This turns out to be a strategic approach in modeling a binary mixture when

no reaction occurs (Di Pasquale et al., 2012; Gavi et al., 2007). In line with the DQMOM-IEM, the weights and weighted abscissas in the two environments 1 and 2 are directly solved through suitable transport equations:

$$\frac{\partial}{\partial \mathbf{x}}\left(\bar{\rho}\langle \mathbf{U}\rangle p_1\right) - \frac{\partial}{\partial \mathbf{x}}\left(\bar{\rho}\Gamma_t \frac{\partial p_1}{\partial \mathbf{x}}\right) = 0, \tag{4}$$

and $p_2 = 1 - p_1$ (the PDF integrates to unity), together with:

$$\frac{\partial}{\partial \mathbf{x}}\left(\bar{\rho}\langle \mathbf{U}\rangle p_1\xi_1\right) - \frac{\partial}{\partial \mathbf{x}}\left(\bar{\rho}\Gamma_t \frac{\partial}{\partial \mathbf{x}}(p_1\xi_1)\right) = \\ = \bar{\rho}\gamma_M p_1 p_2 \left(\xi_2 - \xi_1\right) + \frac{\bar{\rho}\Gamma_t}{\xi_1 - \xi_2}\left(p_1 \frac{\partial \xi_1}{\partial \mathbf{x}}\frac{\partial \xi_1}{\partial \mathbf{x}} + p_2 \frac{\partial \xi_2}{\partial \mathbf{x}}\frac{\partial \xi_2}{\partial \mathbf{x}}\right). \tag{5}$$

The right-hand side of Equation (5) represents the molecular mixing, also referred to as micro-mixing term, mathematically closed with the IEM approach (Fox, 2003); $\gamma_M = \frac{C_\phi}{2}\frac{\varepsilon}{k}$ is the micro-mixing rate, where C_ϕ is a parameter that depends on the local Reynolds number (Fox, 2003) and ε and k are respectively the turbulence dissipation rate and the turbulent kinetic energy. More details can be found in Gavi et al. (2007). By inverting the subscripts 1 and 2, the transport equation related to $p_2\xi_2$ can be obtained. ξ_1 and ξ_2 can be interpreted as local good solvent mass fractions in the two "environments", representing turbulent composition fluctuations. The Favre-averaged mass fraction can be calculated as follows:

$$\langle \xi \rangle = \int_0^1 p(\xi)\xi d\xi \approx p_1\xi_1 + p_2\xi_2, \tag{6}$$

where $p(\xi)$ is the PDF related to the mixture fraction ξ. According to Equa-

tion (6), also the good solvent volume fraction can be defined as:

$$\langle \xi_v \rangle = p_1 \xi_{1,v} + p_2 \xi_{2,v}, \tag{7}$$

where $\xi_{i,v}$ is the volume fraction in the environment $i = 1, 2$, function of the mass fraction through the relation $\xi_{i,v} = [1 + (1/\xi_i - 1) \cdot \rho_s/\rho_w]^{-1}$, with ρ_s and ρ_w the good solvent and water densities, respectively.

2.2. Thermodynamics of real polymers in solution

This section is referred to the thermodynamic model that is incorporated into the PBM-CFD model. Let us recall the Flory theory of real polymers in solution (Flory, 1953). The polymer conformation in a given mixture is the balance between attractive and repulsive forces among the repeated units, taken into account through the so called excluded volume v. The polymer conformation is strictly related to the nature of the solvent and, more specifically, the polymer mean squared radius of gyration, appearing in Eq. (3), can be expressed via the Flory law, that can in turn be extended to molecular clusters or NP containing n polymer molecules, as shown in our previous work:

$$[\![{R_g}^2(n, x_s)]\!] = k_s(x_s)(nM_w)^{2\nu_s(x_s)}, \tag{8}$$

where, as mentioned, the freely-jointed chain hypothesis is applied for a molecular cluster containing n PCL molecules, M_w is the molecular weight of a single PCL molecule and $k_s(x_s)$ and $\nu_s(x_s)$ are the Flory parameters, dependent, in turn, on the good solvent molar fraction x_s and on the nature of the solvent, as indicated by the subscript s. As far as the acetone is

concerned as good solvent, molecular dynamics calculations have been performed and interpolated and the corresponding functional forms determined in a previous work (Di Pasquale et al., 2014):

$$k_s(x_s) = k_{ref}(x_{ref}) = 0.0064 \exp(-3.15 x_{ref}), \tag{9}$$

$$\nu_s(x_s) = \nu_{ref}(x_{ref}) = 0.30 + 0.45 x_{ref} - 0.15 x_{ref}^2, \tag{10}$$

where the subscript 'ref' is introduced and from now on it will refer to as the reference solvent, namely the solvent for which all the necessary information is already provided from previous studies (acetone in this case).

When the repulsive forces dominate on the attractive ones among the monomers, the excluded volume v assumes a positive value and the polymer shows a more stretched (coil) conformation, corresponding to a good solvent condition, and the Flory exponent is equal to 3/5. On the contrary, when the monomer attractive forces prevail, the excluded volume v is negative and the polymer exhibits a globule conformation. The latter case corresponds to a bad solvent condition and the Flory exponent is equal to 1/3. When the two forces counterbalance each other, the excluded volume is null and the polymer assumes an ideal conformation, related to the so called 'θ-condition'. At the θ-condition, the Flory exponent is equal to 1/2. The close proximity to the bad solvent condition is crucial to be locally reached in FNP, in order to induce the spontaneous self-assembly of the polymer molecules in molecular cluster or NP.

As a matter of fact, then, the polymer conformation is strictly depen-

dent on the nature of the surrounding solvent; therefore, the Flory-Huggins interaction parameter, $\chi_{s,p}$, is introduced in this modeling framework, being this one a direct measure of the energetic interaction of two components, e.g, a solute p and a solvent s, in turn, strictly correlated to the solubility of the solute in that specific solvent. The solubility is here taken into account by using the Hansen solubility parameters (HSP). The model presented in this work correlates the radius of gyration with the interaction parameter χ and the HSP, in order to be able to properly define the Flory parameters ($k_s(x_s)$ and $\nu_s(x_s)$) functional forms in Eq. (8), when different good solvents are employed.

Before getting into the HSP theory, a brief mention to the Hildebrand approach is mandatory. The Hildebrand solubility parameter (Hildebrand and Scott, 1950) of a substance corresponds to the cohesive energy per unit volume (it quantifies the work necessary to keep molecules close to each other) and reads as follows:

$$\delta = \left(\frac{\Delta H_v - RT}{V} \right)^{1/2}, \tag{11}$$

where ΔH_v is the vaporization enthalpy, R is the gas constant, T is the absolute temperature and V is the molar volume.

Hansen (2007) proposed a decomposition of the Hildebrand parameter into three different contributions, leading to the so-called Hansen solubility parameters (HSP):

$$\delta = \left(\delta_D^2 + \delta_P^2 + \delta_H^2 \right)^{1/2}, \tag{12}$$

where δ_D considers the dispersion attractive forces (non-polar), δ_P accounts for the permanent dipole-permanent dipole interactions and δ_H for the hydrogen bonds. The main advantage of the HSP approach is that polar effects are explicitly considered, differently from the Hildebrand parameter that is more suitable for apolar systems. The ability of a given solvent to solubilize a solute (e.g., polymer) is expressed in terms of solubility 'distance' from the solute itself and takes the form of the radius of a sphere in Hansen solubility space $\{\delta_D, \delta_P, \delta_H\}$ (Hansen, 2007):

$$Ra^2(\delta) = 4(\delta_{D,s} - \delta_{D,p})^2 + (\delta_{P,s} - \delta_{P,p})^2 + (\delta_{H,s} - \delta_{H,p})^2, \tag{13}$$

where $Ra(\delta)$ is the solubility 'distance', in terms of sphere radius in the Hansen space, and the subscripts s and p refer respectively to the solvent and the polymer. The term '4' is added in order to make the shape of this functional form more spherical and less elliptical. The whole derivation can be found in Hansen (2007). The Flory-Huggins parameter relative to the interaction between the solvent and the polymer $\chi_{s,p}$ can be expressed as a function of the HSP through:

$$\chi_{s,p} = \frac{1}{2} \cdot \left(\frac{Ra(\delta)}{2R_m} \right)^2, \tag{14}$$

where $Ra(\delta)$ is the solubility distance, function of the HSP, as reported in Eq. (13) and R_m represents the radius of the solubility sphere, namely the maximum solubility distance (in Hansen solubility space) that allows the solvent to dissolve the solute. It is worthwhile to stress again that in Hansen phase space the coordinates are square roots of energies per unit volume;

therefore, talking about 'solubility distances' refers implicitly to 'energetic distances' contributions between two components. The parameter R_m is defined in such a way that the dependence of the solubility parameters on the polymer molecular weight is accounted for, thanks to the following expression:

$$R_m^2 = 0.5(1 + 1/r^{1/2})RT/V_m, \tag{15}$$

where V_m is the molar volume of the solvent and r is the degree of polymerization, which can be calculated as the ratio between the total PCL macromolecule and the single repeated unit molecular weights.

Solvents characterized by $Ra > 2R_m$ are classified as non-solvents (or bad solvents) with respect to that specific solute. On the contrary, all the solvents that belong to the Hansen solubility sphere ($Ra/2R_m$ smaller than unity) are classified as good solvents for that solute. In terms of $\chi_{s,p}$ interacting parameter, what stated above is equivalent to infer that when $\chi_{s,p} < 1/2$ the system is in good solvent condition, namely the solute molecule shows a more stretched conformation because the solvent-solute interactions are preferred over the solute-solute ones; $\chi_{s,p} > 1/2$ corresponds to bad solvent condition, namely the solute molecule shows a more globule conformation because the solute-solute interactions are preferred over the solvent-solute ones; $\chi_{sp} = 1/2$ is the θ-condition, corresponding to ideal conformation of the solute molecule occurring when the solute-solvent and solute-solute interactions are energetically equivalent.

As stated above, it is the local close proximity to bad solvent condition that energetically (and also entropically) drives the spontaneous PCL self-

assembly. Under these conditions, the radius of gyration of a single polymer molecule, R_g, can be expressed as a function of the Flory-Huggins parameter, $\chi_{s,p}$ (Rubinstein and Colby, 2003):

$$R_g \approx \frac{b^2}{|v|^{1/3}} N^{1/3} = \frac{bN^{1/3}}{(2\chi_{s,p} - 1)^{1/3}}, \tag{16}$$

where b is the Kuhn length (representative of the monomer length) and N is the number of repeated units that form the polymer chain. The expression reported in Eq. (16) is for real polymers in solution, since the negative excluded volume v is taken into account, as well as the Flory exponent 1/3 appears, meaning that the single polymer molecule is surrounded by a bad solvent.

Starting from the relationship reported in Eq. (14), combined with Eq. (16), the whole procedure to find the Flory parameters functional forms for an unknown good solvent is developed and extensively explained in the following section.

3. Operating conditions and numerical details

3.1. Experimental background

Details about the experimental set-up which this modeling work is based on are here reported. As already stated, PCL is the polymer employed as solute in the FNP process investigated in this work. It is especially suitable for NP production in the pharmaceutical field and for biological applications, since PCL is bio-compatible and non-toxic (Who et al., 2000); among the other advantages, it is also permeable to low molecular weight drugs and can therefore be used for diffusion controlled delivery systems (Le Roy Boehm

et al., 2000). The experimental procedure for PCL NP production has been extensively validated throughout the years (Barresi et al., 2015; Celasco et al., 2014; Ferri et al., 2017; Lavino et al., 2019; Lince et al., 2008, 2009, 2011; Massella et al., 2018; Valente et al., 2012a,b; Zelenková et al., 2015, 2014). In the experimental context, the NP stabilization over time is of paramount importance and, in order to prevent further aggregation at the mixer outlet (Barresi et al., 2015; Saad, 2007) and to preserve the particle size distribution, the outlet CIJM stream is usually quickly diluted in ultra-pure water and gently stirred to stabilize the NP suspension. Dilution, also labelled as 'quench', avoids the size increase due to Ostwald ripening effects (Barresi et al., 2015; Ferri et al., 2017; Zelenková et al., 2015, 2014) and keeps the precipitated NP stable up to 20 days (Le Roy Boehm et al., 2000). The water quench volume can have an effect of the final NP size (Barresi et al., 2015; Ferri et al., 2017), therefore all the experimental data shown here are obtained by quenching with the same water amount.

Although several polymers have been tested for NP production via FNP (Saad, 2007), very little experimental data are available in literature - to the best of the authors knowledge - showing the effect of different good solvents for the same specific type of polymer. As this represents the aim of this work, only experimental studies using PCL as polymer solute have produced enough data to guarantee a consistent comparison with our modeling results.

The experimental measurements were conducted via Dynamic Light Scattering (DLS) in diluted samples. By means of this technique the hydrodynamic radius, R_H, is estimated as the ratio between the 7^{th}- and the 6^{th}-order moments of the NP distribution. However, from our modeling point of view,

those quantities can be determined only with a numerical regression since the highest order moment we solve numerically is of order three (only two nodes in the aggregation model solved via QMOM). Therefore, it turns out to be more reasonable to express the mean particle size in terms of ratio between 1^{st}- and 0^{th}-order moments of the radius of gyration, R_g, distribution. Despite the hydrodynamic radius is generally greater than the radius of gyration (Bhattacharjee, 2016), we made the approximation: $R_H \approx R_g$ which holds particularly for spherical NP. Ultimately, it is an acceptable assumption for narrow CMD characterized by small poly-dispersity indexes (Barresi et al., 2015; Ferri et al., 2017).

3.2. Experimental set up

Four different good solvents are investigated in this work: acetone (ACT), acetonitrile (ACN), tetrahydrofuran (THF) and tert-butanol (TBA). As stated above, the acetone is labelled as the reference solvent, since a full modeling description thereof was already provided from previous molecular dynamics (Di Pasquale et al., 2014) and CFD simulations (Di Pasquale et al., 2012; Lavino et al., 2017). The geometrical dimensions of CIJM are: inlet and outlet diameters respectively equal to 1 and 2 mm. The width of the chamber is equal to 4.76 mm and its height is two times the width, in line with our previous work (Di Pasquale et al., 2012; Lavino et al., 2017).

3.3. Numerical details

According to the quadrature-based moments method employed in this work, the mean radius of gyration of a population of NP is calculated by means of nodes and weights of the quadrature procedure, as reported in

Lavino et al. (2017). The comparison with experiments is done in terms of this value exiting the CIJM. As stated above, during experiments the aggregation is limited and the particles are stabilized by quench water immediately after precipitation, preventing in this way further aggregation. It is reasonable to conclude, therefore, that measuring an average property at the outlet of the mixer from our simulations is totally equivalent to measure experimentally the given property immediately after quenching, via dynamic light scattering. However, it is worthwhile to mention that uncertainties present in the current work and the derivation of the models (Flory parameters, aggregation kernel, etc.) keep the predicted NP dimensions always included into the uncertainty range of the experimental results (Ferri et al., 2017; Lavino et al., 2017).

It is important to stress here that the choice of the good solvent has multiple effects on the FNP process. Indeed, by changing the good solvent we simultaneously change the thermodynamics of the interaction between the polymer chains and the good solvent and bad solvent mixture, the kinetics of polymer molecule self-assembly and the dynamics of mixing of the two feed streams (i.e., good and bad solvent). As mentioned in the introduction, the main objective of this work is to quantify each of these effects (on the final NP size and CMD) separately.

Density, viscosity and molar volume of the good solvents represent the physical-chemical properties that are expected to play a role in the FNP process. The density of the good solvent affects the fluid dynamics in the CIJM and the position of the impinging plane. The viscosity of the good solvent determines, via the Stokes-Einstein law already included in the aggregation

kernel reported in Eq. (3), the kinetics of molecules and molecular cluster self-assembly/aggregation. The molar volume of the good solvent defines the final good solvent molar fraction (for a given volume ratio between good and bad solvents). They are schematically listed in Table 1.

Table 1: Physical-chemical properties of the good solvents and Reynolds number, Re_s, range investigated in this work. Re_s refers to the good solvent inlet jet stream (see Eq. (17)).

Good solvent	**Density, kg m^{-3}**	**Viscosity, Pa·s**	**Molar volume, cm^{3}mol^{-1}**	**Re$_s$ range**
ACT	780.85	3.10×10^{-4}	74.38	1069 – 6414
ACN	771.45	3.26×10^{-4}	53.21	1004 – 6026
THF	874.78	4.34×10^{-4}	82.43	855 – 5133
TBA	777.89	3.46×10^{-3}	95.29	95 – 573

As it can be seen in Table 1, acetone and acetonitrile have similar values of density and viscosity; instead, acetonitrile has a smaller molar volume; this may become a crucial factor that affects the mean NP size, as it will be shown in section 4. On the contrary, THF has higher density, viscosity and molar volume with respect to acetone and acetonitrile. More generally, despite all the solvents investigated here present similar physical properties, it is noteworthy to stress that TBA exhibits one order of magnitude higher viscosity. The way in which the density fluctuations are taken into account, as well as the local viscosity and molar fraction dependence on molar volumes, are reported in an our previous work (Lavino et al., 2017), and therefore here omitted for the sake of brevity.

Although experiments and simulations are conducted by varying the inlet flow rate, the mean radius of gyration of the NP exiting the CIJM is evaluated as a function of Reynolds number, Re_s, referred to the good solvent inlet jet

stream and its definition reads as follows:

$$\mathrm{Re_s} = \frac{\rho_s d_{in} u_j}{\mu_s} \tag{17}$$

where d_{in} is the CIJM inlet diameter, u_j is the mean inlet jet velocity, ρ_s and μ_s are the good solvent density and viscosity respectively, as reported in Table 1. When comparing the dynamics of aggregation for different good solvents, the Reynolds number includes the inlet operating conditions as well as the physical properties of the good solvent to make the outcome of this work a general discussion, as it will be clearer in section 4.

Solvents and polymer Hansen solubility parameters (HSP), as well as the corresponding distances from PCL, Ra, are listed in Table 2.

Table 2: Hansen solubility parameters (HSP) and distances, Ra, from PCL (Eq. (13)) for all the components of the investigated system.

	δ_D, MPa$^{1/2}$	δ_P, MPa$^{1/2}$	δ_H, MPa$^{1/2}$	Ra, MPa$^{1/2}$
PCL	17.0	4.8	8.3	-
THF	16.8	5.7	8.0	1.0
ACT	15.5	10.4	7.0	6.5
TBA	15.2	5.1	14.7	7.4
ACN	15.3	18.0	6.1	13.8
Water	15.6	16.0	42.3	35.9

The distances from PCL are representative of the solvent affinity with the polymer. More specifically, the lower is the distance (last column in Table 2), the higher is the solvent-solute affinity. As expected, the water solubility distance is the highest value, much higher than the Hansen solubility sphere radius for PCL, $R_m \approx 9.8$ MPa$^{1/2}$ (calculated by means of swelling tests Bordes et al. (2010)), proving therefore to behave as bad solvent. In

the Hansen phase space, acetone, THF and TBA belong to the Hansen solubility sphere, behaving as good solvents. In the case of acetonitrile, the distance from PCL is shown to be slightly higher than the sphere radius. It is worthwhile mentioning that Bordes et al. (2010) obtained this value of R_m by performing swelling tests in which PCL initial concentration was two orders of magnitude higher than the one employed in this work. It is therefore reasonable to assume that R_m would be much higher in this context, so that also acetonitrile leads to a full PCL solubilization, as seen in our experiments (Ferri et al., 2017), and consequently behaving as good solvent in these operating conditions.

In this analysis, the solute is the PCL and the solvent is the 'good solvent-water' mixture. Being the second phase made by a binary mixture, all the solubility parameters (e.g., HSP) and physical properties (e.g., molar volume) involved in the following calculations are weighted on the good-bad solvents volume and molar fractions. The binary mixture phase will be therefore generically labelled as 'solvent' from now on. The single PCL macro-molecule molecular weight $M_w = 14000$ g mol^{-1} and the repeated unit molecular weight $M_o = 114$ g mol^{-1}. The term r appearing in Eq. (13) corresponds to the degree of polymerization, here simply evaluated as M_w/M_o.

Let us recall that in FNP the PCL solubility limit is overcome and the self-assembly induced only thanks to the presence of the bad solvent, which is a local effect. Furthermore, the mixing is generally very fast and efficient, leading to a well micro-mixed system in almost all the domain of the CIJM (Gavi et al., 2007). Hence, the assumption of considering the polymer chain at the mean good solvent molar fraction $\bar{x}_s$ holds, after mixing occurs, in

the range $\bar{x}_s \in [0.15, 0.25]$ for all the good solvents, since the good solvent-to-water ratio in volume is constant and equal to unity. Consequently, the three-components phase diagram (water, good solvent and PCL) can be approximated as a two-components one (the polymer as solute and the binary mixture as solvent) (Flory, 1953). In these conditions, the single PCL radius of gyration dependence on $\chi_{s,p}$ can be expressed by means of Eq. (16), since the binary mixture behaves as a bad solvent, leading the single macromolecules to self-assemble. This concept will be confirmed by looking at the $\chi_{s,p}$ values, reported in Table 3 later on.

By using the relation reported in Eq. (16) for two different solvents $s1$ and $s2$ (e.g., $s1$ = acetonitrile-water and $s2$ = acetone-water), and assuming that the Kuhn length b (mainly a solute property) does not change too much for any solvent used, the following ratio can be readily obtained:

$$\frac{[\![R_g(n=1)]\!]_{s1}}{[\![R_g(n=1)]\!]_{s2}} \approx \frac{(2\chi_{s2,p}-1)^{1/3}}{(2\chi_{s1,p}-1)^{1/3}} = S_f, \tag{18}$$

where S_f is a scaling ratio, function of the solely Flory-Huggins parameters $\chi_{s1,p}$ and $\chi_{s2,p}$, calculated starting from the HSP through Eq. (14). The adopted strategy consists in setting $s2$ as the reference solvent, i.e., acetone-water in this case, for which the functional forms of Flory parameters are known from MD (Di Pasquale et al., 2014). By rearranging Eq. (18) as a function of the reference solvent, the following equality holds:

$$\sqrt{k_{s1}(x_{s1})M_w^{2\nu_{s1}(x_{s1})}} = S_f \cdot \sqrt{k_{ref}(x_{ref})M_w^{2\nu_{ref}(x_{ref})}}, \tag{19}$$

where, as stated above, the subscript ref refers to the acetone-water mix-

ture. Scaling factors S_f and Flory-Huggins parameters $\chi_{s,p}$ referred to the solvent-polymer systems investigated in this work, namely acetone-water, acetonitrile-water, THF-water and TBA-water, evaluated at mean good solvent molar fraction $\bar{x}_s$, are reported in Table 3.

Table 3: Flory-Huggins parameter, $\chi_{s,p}$, for acetone, acetonitrile, THF and TBA as good solvents with the relative scaling factors obtained from Eq. (18), at mean good solvent molar fraction, $\bar{x}_s$.

Solvent	$\bar{x}_s$	**Flory-Huggins parameter**, $\chi_{s,p}$	**Scaling factor**, S_f
ACT-water	0.20	0.926	1.00
ACN-water	0.25	1.007	0.94
THF-water	0.18	0.873	1.05
TBA-water	0.16	1.251	0.83

By looking at Table 3, the Flory-Huggins parameter is always greater than 1/2 (θ-condition) for each solvent investigated here. This confirms what was already stated above: the systems are in bad solvent conditions and the single PCL macromolecules are spontaneously led to aggregate.

At this point, an iterative procedure can be carried out, based on Eq. (19) and on the values reported in Table 3. More specifically, Eq. (19) still presents two degrees of freedom, that are the Flory constant and exponent functional forms. By putting $\nu_{s1}(x_{s1}) = \nu_{ref}(x_{s1})$ as starting value, $k_{s1}(x_{s1})$ is univocally determined and with this new set of Flory parameters, say $k^*_{s1}(x_{s1})$ and $\nu^*_{s1}(x_{s1})$, simulations can be performed and the deviation against the experimental data is detected. Based on the deviation with respect to experiments, the Flory exponent is suitably adjusted to a new functional form, say $\nu^{**}_{s1}(x_{s1})$ and, by means of Eq. (19), a new functional form for $k^{**}_{s1}(x_{s1})$ is obtained. With this new set of Flory parameters, simulations are performed until this

iterative procedure leads to an acceptable accordance against experiments. This corresponds to the Flory parameters reported in Table 4.

Table 4: Flory parameters functional forms for acetone (reported in Eq. (9) and (10)), acetonitrile, THF and TBA.

Good solvent	$k_s(x_s)$	$\nu_s(x_s)$
ACT	$0.0064\exp(-3.15x_s)$	$0.30+0.45x_s-0.15x_s^2$
ACN	$0.0055\exp(-3.15x_s)$	$0.30+0.40x_s-0.10x_s^2$
THF	$0.0047\exp(-3.15x_s)$	$0.30+0.62x_s-0.32x_s^2$
TBA	$0.0056\exp(-3.15x_s)$	$0.30+0.42x_s-0.12x_s^2$

The adjustment of the Flory parameters functional forms deserves further explanations. Regarding the Flory constant, $k_s(x_s)$, only the proportionality constant of the exponential is adjusted with respect to the function referred to acetone, Eq. (9). As far as the Flory exponent $\nu_s(x_s)$ is concerned, it corresponds to a parabolic profile (Eq. (10)); therefore, three conditions are needed: two of them are represented by the exponent value in pure good and pure bad solvent, that are respectively 3/5 and 1/3, in line with the Flory theory. The third condition is the only degree of freedom that the user needs to fulfill and it might correspond to its value at the mean good solvent molar fraction, $\nu_s(\bar{x}_s)$, that is suitably adjusted during the iterative procedure presented above.

4. Results

First, only the dynamics of mixing is shown in order to assess the importance of changes in physical properties when different good solvents are used in FNP. In Figure 1 two quantities related respectively to macro- and micro-mixing are reported for all the four solvents investigated here and for

two feeding flow rates. The first one is represented by the good solvent volume fraction, $\langle \xi_v \rangle$ (see Eq. (7)). It is clear how in general the macro-mixing is very efficient for all the solvents since in almost the whole domain $\langle \xi_v \rangle$ approaches to 0.5, as expected by using an inlet volume flow rate ratio equal to unity. Two different flow rates are here considered: 40 mL/min and 100 mL/min. Further mathematical details about the macro-mixing are reported in Appendix A.

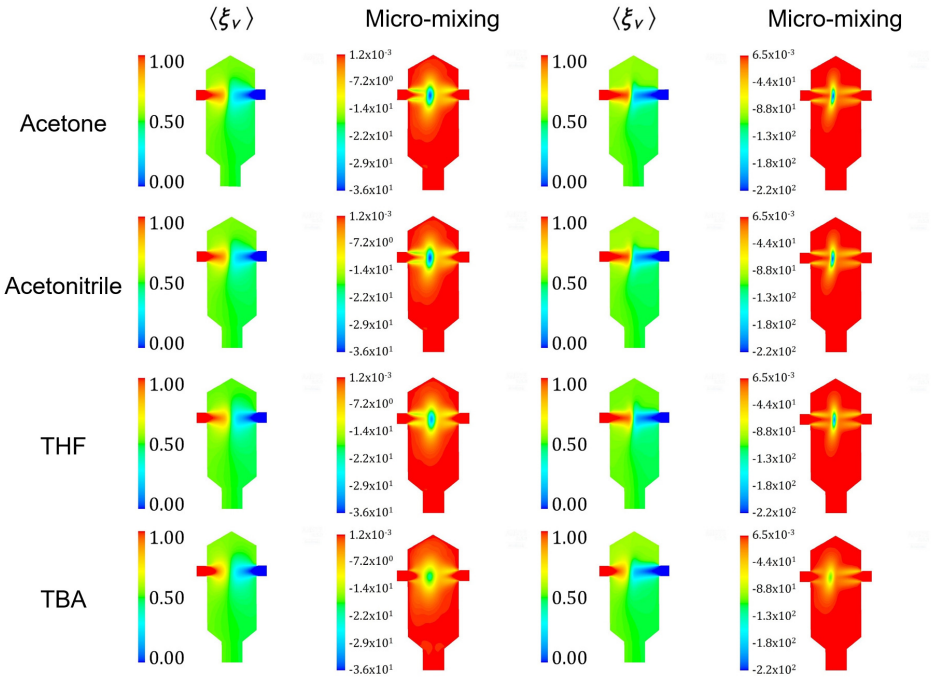

Figure 1: Good solvent volume fraction, $\langle \xi_v \rangle$ (Eq. (7)), and micro-mixing term, $\gamma_M p_1 p_2 (\xi_2 - \xi_1)$ (Eq. (A.4)), for which a further mathematical and physical analysis is reported in section 2.1 and in Appendix A. Two inlet flow rates are here reported: 40 mL min^{-1} (left side) and 100 mL min^{-1} (right side).

Besides macro-mixing, it is worthwhile to evaluate also the micro-mixing, being this one a fundamental aspect of FNP (Di Pasquale et al., 2012). As already mentioned, the mixture fraction is modeled via the DQMOM-IEM for which the corresponding transport equation is reported in section 2.1. A particular focus is given now to the micro-mixing term of that transport equation which corresponds to $\gamma_M p_1 p_2 (\xi_2 - \xi_1)$, where γ_M is the micro-mixing rate, namely expressing the rate with which good solvent and bad solvent mix at the molecular level. p_i and ξ_i correspond respectively to the weights and abscissas (or nodes, or environments) of the quadrature formula, in the two environments $i = 1, 2$, in line with the DQMOM approach (Marchisio and Fox, 2005). The whole micro-mixing term describes how fast the micro-mixing variance is dissipated by turbulence (Fox, 2003; Liu and Fox, 2006). The entire mathematical framework is here omitted, being already presented in our previous works (Di Pasquale et al., 2012; Lavino et al., 2017) and a further mathematical elaboration is provided in Appendix A, in which the relationship between micro-mixing term and micro-mixing variance is clearly stated.

At this level of description, Figure 1 points out that the micro-mixing term is very similar for acetone, acetonitrile and THF; a different trend is detected for TBA, for which micro-mixing turns out to be less efficient compared with the other good solvents. It is noteworthy to stress here that the numerical values in the contour plots must be interpreted as absolute values, since negative terms may come out from the local value of the abscissas in the two environments of the quadrature. Indeed, this is proven by looking at the region in which the turbulence is created and dissipated, which is where

molecular-mixing or micro-mixing occurs. It is clearly less shrunk around the impinging plane than in other solvents, showing wider spatial gradients in the mixer domain. This might be induced by the viscosity that in the case of TBA is shown to be much larger (one order of magnitude) than in the other solvents. These results, by just looking at the mixing dynamics of the system, already allows us to predict a different scenario for TBA with respect to acetone, acetonitrile and THF.

Let us move now on the dynamics of aggregation. In the case of the first three solvents (i.e., acetone, acetonitrile, THF), whose dynamics of mixing, only depending on their physical properties, is shown to be the same, it is worthwhile to conduct the following analysis. For the sake of brevity, let us consider only acetone and a 'virtual' solvent, characterized by the acetonitrile physical properties (Table 1) and by acetone functional forms of Flory parameters, namely Eq. (9) and (10). By simulating these two solvents with the solely Brownian aggregation kernel active, we can quantify the dynamics of self-assembly of polymer molecules into clusters and of small clusters into larger clusters (before turbulent aggregation takes over). Although the same functional forms of the acetone Flory parameters are considered here also for the 'virtual' solvent, the results show a very different profile, in terms of mean radius of gyration of the NP at the outlet of the mixer. This result is depicted in Figure 2 and tells us that, although the dynamics of mixing is identical between acetone and the 'virtual' solvent, the aggregation behaves in a very different way. The only physical explanation of that is attributable to one physical property and, more specifically, lies on the different molar volumes of the two solvents (look at Table 1), because the other

physical properties (density and viscosity) are very similar to each other, as also demonstrated by looking at the respective Reynolds number values (see Table 1). The molar volumes affect the molar fraction of the mixture, x_s, as reported in Table 3 concerning its mean value, after mixing takes place. The Flory parameters functional forms are, in turn, function of molar mixture fraction. This analysis demonstrates that the differences between good solvents about the dynamics of aggregation only depend on Flory parameters. Furthermore, it is shown how the modeling approach presented in this work can be suitably employed to quantify the relative importance of the different mechanisms involved in particles formation.

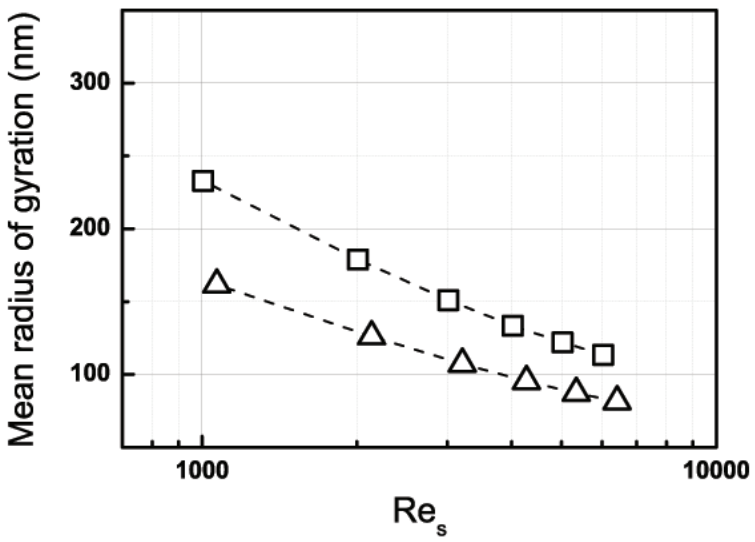

Figure 2: Mean radius of gyration as a function of Reynolds number referred to the good solvent inlet jet stream, with only Brownian aggregation for PCL initial concentrations equal to 6.0 mg/mL in acetone (triangles) and the 'virtual' solvent (squares), characterized by the acetonitrile physical properties and by the acetone functional forms of Flory parameters.

At this point of the current analysis, it is straightforward that the gap against experiments must be bridged by suitably adjusting the functional forms for $k_s(x_s)$ and $\nu_s(x_s)$ for all the solvents investigated here. As outcome of the iterative procedure presented in section 3 (see Eqs. (18) and (19) and Table 3), the final functional forms of the Flory parameters are determined and listed in Table 4. These new functional forms are able to guarantee a good agreement with experiments, as depicted in Figure 3 (TBA- and THF-water systems) and Figure 4 (acetone- and acetonitrile-water systems). The range of PCL initial concentrations in the good solvent stream spans from 3.0 to 9.0 mg mL^{-1}. The experimental error bars are also included.

Note that the accordance of the current model with experiments is in line with the results found out in our previous work (Lavino et al., 2017). As far as acetone, acetonitrile and THF are concerned, the agreement is excellent starting from medium PCL initial concentration in good solvent stream of about 5 mg/mL, namely the predicted NP dimensions are included into the uncertainty range of the experimental results. In the case of TBA, where the mixing dynamics is less efficient than in the other three good solvents, the model shows to be transferable, by means of the Flory-Huggins solubility theory. The experimental profile is qualitatively caught by this purely-aggregative model, reproducing the negligible effect of the kinetics on the final mean radius of gyration (flat profile of NP size as function of the inlet good solvent Reynolds number) (Johnson and Prud'homme, 2003b; Zelenková et al., 2015). This behaviour is also explained by looking at the Re_s range experienced by TBA in FNP with respect to the other systems, as clearly shown in Figures 3 and 4. Indeed, Re_s ranges of acetone, acetonitrile,

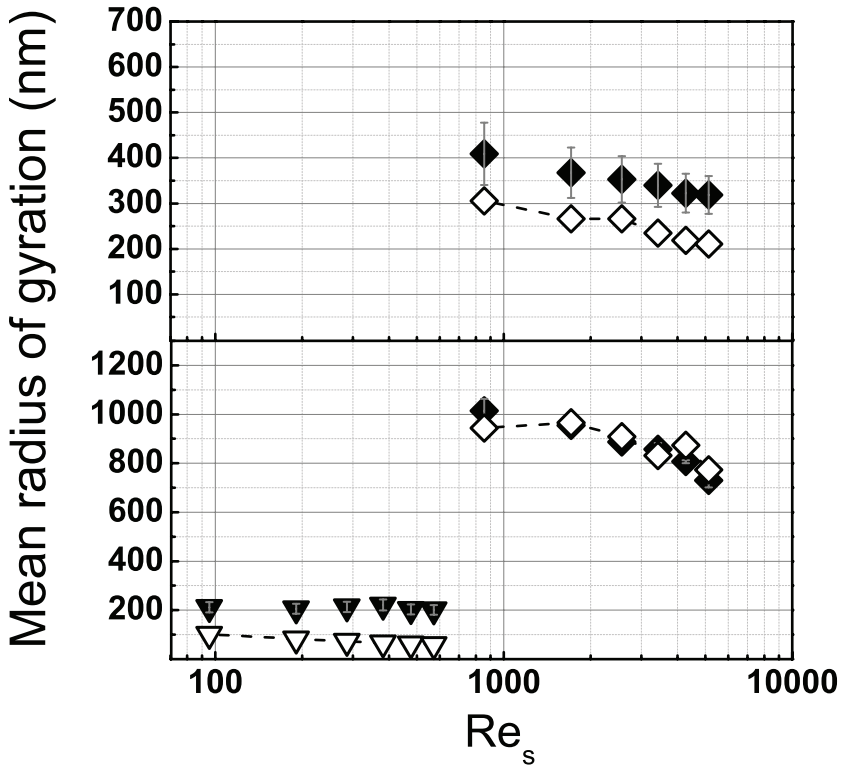

Figure 3: Mean radius of gyration of the NP exiting the CIJM versus the Reynolds number referred to the good solvent inlet jet stream as measured in experiments (black symbols) and as predicted by the purely-aggregative model (dashed line, empty symbols) for PCL-14000 initial concentrations equal to 3.0 (top panel) and 5.0 (bottom panel) mg/mL in THF (diamonds) and TBA (inverted triangles).

and THF are almost the same as well as one order of magnitude higher than TBA inlet Reynolds number, mainly due to the TBA viscosity (see Table 1). In the case of TBA, Re_s value presumes that the turbulence is not completely developed inside the CIJM leading to less efficient mixing dynamics - as already stated - and, therefore, to a less important effect of fluid dynamics on the final mean NP size with respect to the other good solvent systems, as reproduced by both experiments and simulations. Results show,

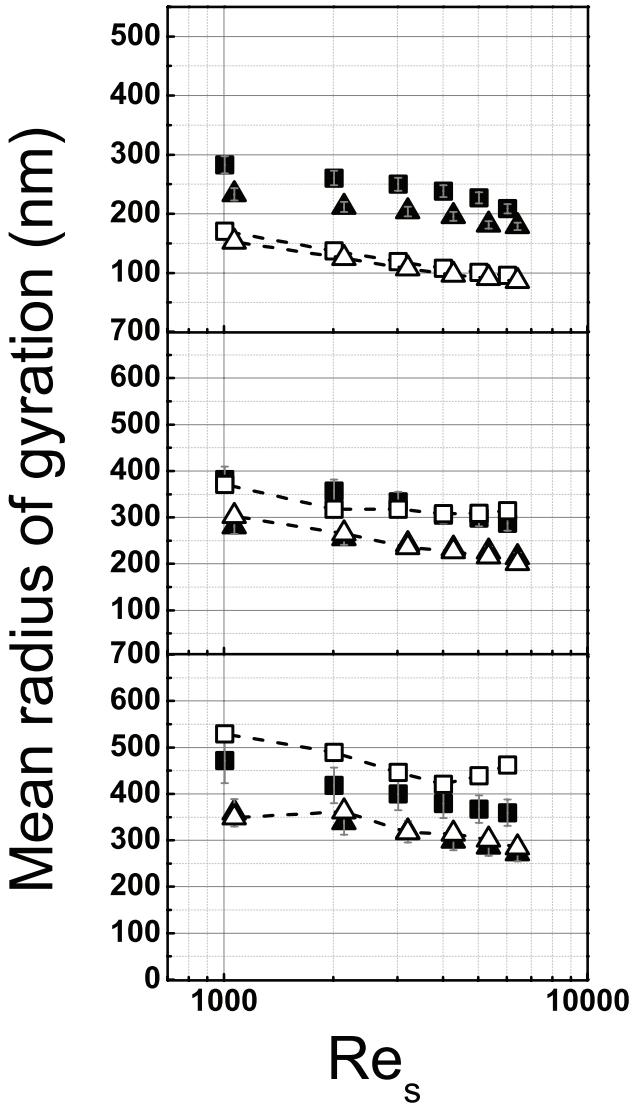

Figure 4: Mean radius of gyration of the NP exiting the CIJM versus the Reynolds number referred to the good solvent inlet jet stream as measured in experiments (black symbols) and as predicted by the purely-aggregative model (dashed line, empty symbols) for PCL-14000 initial concentrations equal to 3.0 (top), 6.0 (middle) and 9.0 (bottom) mg/mL in acetone (triangles) and acetonitrile (squares) as the good solvents.

however, a quantitative gap against experiments, which, on the contrary, is not observed in the case of THF (bottom panel in Figure 3) at the same PCL initial concentration (5 mg/mL). It is worthwhile to stress that this gap cannot be numerically overcome by using the proposed computational tuning (described in section 3, in order not to break the physics of the system, namely having higher values of Flory parameters for TBA than in acetone (look at Figure 5) which, instead, is shown to have a better affinity with PCL (lower solubility distance in Hansen phase space). This gap must be therefore related to another phenomenon, as for example the role of nucleation, here neglected (Lavino et al., 2017)). At constant PCL inlet concentration (around 5 mg/mL), nucleation might be more important for TBA than in the other systems, in which turbulence is demonstrated to play a secondary role in the aggregation for PCL inlet concentration under 5 mg/mL by our previous CFD analysis (Lavino et al., 2017).

The Flory exponent profiles (Table 4) are depicted in Figure 5. The inset shows the ν_s values corresponding to the different mean good solvent molar fractions $\bar{x}_s$ (discrete symbols), assuming the perfect mixing between the good and the bad solvent streams, already mentioned in the section 3. This perfect mixing condition corresponds to a single good solvent volume fraction value of 0.5 but different molar fractions, due to the different molar volumes of the good solvents. It is important to point out here that, from a qualitative point of view, the effect of the good solvent on the final mean NP size can be predicted looking at the Flory exponent evaluated at the mean good solvent molar fraction $\nu_s(\bar{x}_s)$. At the mean good solvent molar fraction $\bar{x}_s$, the inset shows the following relation for different good solvents:

682 $\nu_{\mathrm{THF}}(\bar{x}_{\mathrm{THF}}) > \nu_{\mathrm{ACN}}(\bar{x}_{\mathrm{ACN}}) > \nu_{\mathrm{ACT}}(\bar{x}_{\mathrm{ACT}}) > \nu_{\mathrm{TBA}}(\bar{x}_{\mathrm{TBA}})$. This justifies,
683 indeed, the fact that PCL aggregates more in THF than in acetonitrile, in
684 acetone and finally in TBA at constant PCL inital concentration, in line
685 with experiments (Ferri et al., 2017; Zelenková et al., 2015). Therefore,
686 the approach described here is able to reproduce the experimental evidences
687 highlighting the fundamental role played by the good solvent molar fraction.
688 Note that the $\nu_s(\bar{x}_s)$ values are very close to each other, denoting the high
689 sensitivity of the Flory exponent on final mean NP size.

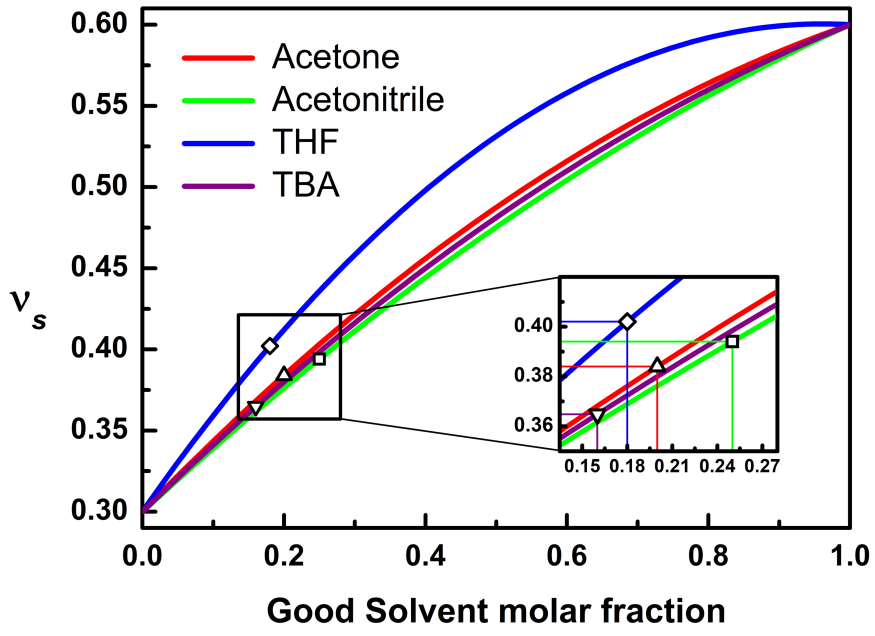

Figure 5: Flory exponent ν_s profiles in function of good solvent molar fraction for acetone (red), acetonitrile (green), THF (blue) and TBA (purple) (Table 4). The discrete symbols correspond to the Flory exponent at the outlet mean good solvent molar fraction $\nu_s(\bar{x}_s)$ (inset).

Figure 5 also depicts the affinity order found out in terms of HSP and solubility distance from PCL shown in Table 2, namely THF > ACT > TBA > ACN for which the solubility distances from PCL are respectively 1.0, 6.5, 7.4 and 13.8 $MPa^{1/2}$. Hence, at constant molar fraction, ν_s is directly proportional to the good solvent affinity with PCL (in terms of solubility distance). This implies that the polymer chain increases in size and assumes a more stretched conformation, according to the thermodynamics of real polymers in solution. However, operating at constant good-solvent-to-water ratio in volume leads to a mean good solvent molar fraction in the order: $\bar{x}_{\mathrm{ACN}} > \bar{x}_{\mathrm{ACT}} > \bar{x}_{\mathrm{THF}} > \bar{x}_{\mathrm{TBA}}$, because of the different molar volumes of the good solvents. This affects the Flory parameters and, consequently, aggregation, the final NP size and CMD.

In Figure 6 the mean-squared radius of gyration of a NP is reported for acetone (red), acetonitrile (green), THF (blue) and TBA (purple) in function of the aggregation number. The crossover between the red and green profiles (acetone and acetonitrile) shows the two different tendencies and contributions in case of single PCL molecule ($[\![R_g(n=1)]\!]$ higher in acetone) and at high aggregation number, n, in which $[\![R_g(n)]\!]$ is higher in acetonitrile than in acetone. This means that, despite the single PCL macromolecule occupies a smaller volume in acetonitrile, the PCL NP is bigger in acetonitrile, namely more PCL macromolecules form the same cluster (or NP) in acetonitrile ($m^{(1)}/m^{(0)}$ is therefore greater than in acetone). Therefore, the Flory theory combined together with the solubility affinity with PCL implies the following order of the single PCL macromolecule dimension: THF > ACT > ACN > TBA, as also indicated by

the S_f values in Table 3. However, the combination of good solvent molar volume (leading to different molar fractions) and the aggregation kernels (dependent on Flory parameters) produces the following aggregation order: THF > ACN > ACT > TBA.

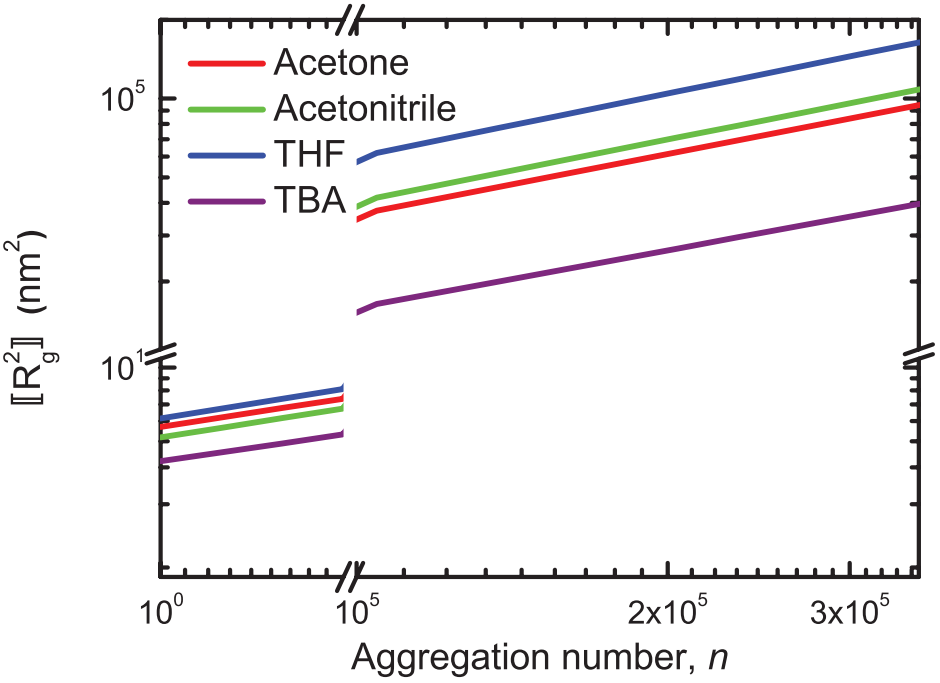

Figure 6: Mean squared radius of gyration, $[\![{R_g}^2]\!]$, as a function of the number of molecules (Eq. (8)) that form a cluster (aggregation number, n) for acetone (red), acetonitrile (green), THF (blue) and TBA (purple) at the respective outlet mean good solvent molar fraction $\bar{x_s}$.

5. Conclusions

In this work the effect of different good solvents in flash nano-precipitation (FNP) is studied, from a modeling point of view. A population balance model (PBM) based on molecules as building blocks is coupled with computational

fluid dynamics (CFD) and implemented in a commercial CFD code. Moments of the cluster mass distribution (CMD) are transported and closed by using the quadrature method of moments (QMOM) (Marchisio and Fox, 2013). The CMD is defined in such a way that it represents the number of polymer molecules inside a cluster/NP. The turbulent mixing effects on NP formation are accounted for with the direct quadrature method of moments coupled with the interaction and exchange with the mean (DQMOM-IEM) method, in line with our reference work, in which this modeling approach was tested and validated (Lavino et al., 2017).

The novelty of the current approach consists in coupling PBM and CFD with thermodynamics of polymers in solution. More specifically, the Flory-Huggins interaction parameter χ is considered, taking into account therefore the energetic contribution related to the polymer in the mixture, and is here correlated to the prediction of the mean radius of gyration of the NP. All this is done by taking advantage of the solubility theory in mixtures, in terms of Hansen solubility parameters (HSP). In this way, different good solvents are studied, with water as anti-solvent and poly-ε-caprolactone (PCL) as solute, in confined impinging jets mixer (CIJM). Four different good solvents are considered: acetone (ACT), acetonitrile (ACN), tetrahydrofuran (THF) and tert-butanol (TBA), taking the acetone as the reference solvent, being this one already investigated at the molecular scale with molecular dynamics in a previous work (Di Pasquale et al., 2014).

Thanks to the proposed approach, kinetics and thermodynamics are intertwined in a unique modeling tool used to investigate separately the dynamics of mixing from the dynamics of aggregation, addressing the main

factors that play a key role in such a complex process. CFD simulations demonstrate that acetone, acetonitrile and THF are characterized by the same macro- and micro-mixing dynamics, whereas TBA shows a different micro-mixing behaviour, strongly dependent on its viscosity, that is one order of magnitude higher than the other solvents and water. Results also show that the molar volume, combined together with the HSP, provides a good prediction of the final mean NP size when different good solvents are employed in FNP. Furthermore, functional forms for the Flory parameters are determined, by combining the Flory-Huggins solubility theory with a suitable computational tuning. In this way, it is shown that the proposed modeling approach is transferable and adaptable to different scenarios, leading to a good prediction of the experimental results from quantitative and qualitative points of view. This is valid also in the case of TBA which presents a different mixing dynamics that, in turn, affects the final NP profile in function of the inlet Reynolds number. The detected limitations, in terms of accordance with experiments, might be overcome by introducing nucleative effects in the aggregation source term of the PBM. In conclusion, although the phenomena involved are very complex and this is not indeed the ultimate model for FNP, this model is able to capture the main effects experimentally observed since both kinetics and thermodynamics are considered.

Future work may be done by investigating these good solvent-water systems at the molecular scale with full-atom and coarse-grained molecular dynamics simulations, aiming at confirming or refining the results obtained in this work, with more detailed molecular models.

Appendix

Appendix A. Mixing modeling and micro-mixing variance

In this appendix, further mathematical details concerning the mixing modeling are provided. More specifically, it will be shown how the micro-mixing variance can be related to the mixing transport equation, in particular to one of its terms: the micro-mixing term. In this modeling framework, as reported in the main text, the mixture fraction is transported by means of the direct quadrature method of moment coupled with the interaction and exchange with the mean method (DQMOM-IEM) (Marchisio and Fox, 2013).

Besides the micro-mixing model introduced in the main text in section 2.1, a large-scale or macro-scale variance $\langle \xi'^2 \rangle_{macro}$ is defined as follows:

$$\langle \xi'^2 \rangle_{macro} = (\langle \xi \rangle - \bar{\xi})^2, \tag{A.1}$$

quantifying how different the local mean mixture fraction $\langle \xi \rangle$ is from the ideal value $\bar{\xi}$ that it would assume if the mixing were perfect. In the analyzed case, for instance, $\bar{\xi}_v = 0.5$ in volume. For the analyzed cases, this tells us that the macro-mixing is very efficient, leading the macro-mixing variance to zero in almost all the CIJM, as shown in Figure 1.

The micro-mixing variance is defined as (Liu and Fox, 2006):

$$\langle \xi'^2 \rangle = \langle \xi^2 \rangle - \langle \xi \rangle^2. \tag{A.2}$$

We can rearrange the last expression as follows:

$$\langle \xi'^2 \rangle = \langle \xi^2 \rangle - \langle \xi \rangle^2 = p_1\xi_1^2 + p_2\xi_2^2 - (p_1\xi_1 + p_2\xi_2)^2 =$$
$$= p_1\xi_1^2(1-p_1) + p_2\xi_2^2(1-p_2) - 2p_1p_2\xi_1\xi_2 =$$
$$= p_1p_2(\xi_1^2 + \xi_2^2 - 2\xi_1\xi_2) = p_1p_2(\xi_2 - \xi_1)^2, \quad \text{(A.3)}$$

where the property $p_1 = 1 - p_2$ is applied. By using the results shown in Eq. (A.3), the first term on right hand side of Eq. (5) that contains the micro-mixing rate can be expressed as follows (the fluid density $\bar{\rho}$ is here omitted for simplicity of notation):

$$\gamma_M p_1 p_2 \, (\xi_2 - \xi_1) = \frac{\gamma_M}{(\xi_2 - \xi_1)} \langle \xi'^2 \rangle, \quad \text{(A.4)}$$

strictly dependent on the micro-mixing variance $\langle \xi'^2 \rangle$. The quantity expressed in Eq. (A.4) is the one reported in the contour plots in Figure 1 and can be thought of as a measure of how the micro-mixing variance is dissipated by turbulence (included in the definition of γ_M) at the micro-scale.

Acknowledgements

This contribution was identified by R. Bertrum Diemer Jr (University of Delaware) as the Best Presentation in the session "Population Balance Modeling for Particle Formation Processes: Nucleation, Aggregation and Breakage Kernels" of the 2018 AIChE Annual Meeting in Pittsburgh. Computational resources were provided by HPC@POLITO, a project of Academic Computing within the Department of Control and Computer Engineering at the Politecnico di Torino (http://www.hpc.polito.it).

References

Andersson, B., Andersson, R., Hakansson, L., Mortensen, M., Sudiyo, R., van Wachem, B., 2012. Computational Fluid Dynamics for Engineering. Cambridge: Cambridge University Press.

Baldyga, J., Orciuch, W., 2001. Some hydrodynamic aspects of precipitation. Powder Technology 121, 9–19. doi:https://doi.org/10.1016/S0032-5910(01)00368-0.

Barresi, A.A., Vanni, M., Fissore, D., Zelenková, T., 2015. Thakur VK, Thaku MK. Handbook of Polymers for Pharmaceutical Technologies. Hoboken: John Wiley & Sons, Ltd. chapter Synthesis and preservation of polymer nanoparticles for pharmaceutical applications. pp. 229–280. doi:https://doi.org/10.1002/9781119041412.ch9.

Bhattacharjee, S., 2016. Dls and zeta potential – what they are and what they are not? Journal of Controlled Release 235, 337 – 351. doi:https://doi.org/10.1016/j.jconrel.2016.06.017.

Bordes, C., Fréville, V., Ruffin, E., Marote, P., Gauvrit, J.Y., Briançon, S., Lantéri, P., 2010. Determination of poly(ε-caprolactone) solubility parameters: Application to solvent substitution in a microencapsulation process. International Journal of Pharmaceutics 383, 236–243. doi:https://doi.org/10.1016/j.ijpharm.2009.09.023.

Celasco, E., Valente, I., Marchisio, D.L., Barresi, A.A., 2014. Dynamic light scattering and x-ray photoelectron spectroscopy characterization of pegylated polymer nanocarriers: Internal structure and surface properties. Langmuir 30, 8326–8335. doi:https://doi.org/10.1021/la501198v.

Cheng, J.C., Vigil, R.D., Fox, R.O., 2010. A competitive aggregation model for flash nanoprecipitation. Journal of Colloid and Interface Science 351, 330–342. doi:https://doi.org/10.1016/j.jcis.2010.07.066.

Choi, Y.J., Chung, S.T., Oh, M., Kim, H.S., 2005. Investigation of cristallization in a jet y-mixer by a hybrid computational fluid dynamics and process simulation approach. Cristal Growth & Design 5, 959–968. doi:https://doi.org/10.1021/cg049670x.

Das, M., Saxena, N., Dwivedi, P.D., 2009. Emerging trends of nanoparticles application in food technology: Safety paradigms. Nanotoxicology 3, 10–18. doi:https://doi.org/10.1080/17435390802504237.

Demetzos, C., 2016. Pharmaceutical Nanotechnology. Singapore: Adis.

Di Pasquale, N., Marchisio, D.L., Barresi, A.A., 2012. Model validation for precipitation in solvent-displacement processes. Chemical Engineering Science 84, 671–683. doi:https://doi.org/10.1016/j.ces.2012.08.043.

Di Pasquale, N., Marchisio, D.L., Barresi, A.A., Carbone, P., 2014. Solvent structuring and its effect on the polymer structure and processability: the case of water-acetone poly-ε-caprolactone mixtures. Journal of Physical Chemistry B 118, 13258–13267. doi:https://doi.org/10.1021/jp505348t.

Elimelech, M., Gregory, J., Jia, X., Williams, R., 1998. Particle Deposition and Aggregation: Measurement, Modelling and Simulation. Woburn: Butterworth-Heinemann.

Favre, A., 1965. Equations des gaz turbulents compressibles i. formes générales. Journal de Mecanique 4, 361–390.

Ferri, A., Kumari, N., Peila, R., Barresi, A.A., 2017. Production of menthol-loaded nanoparticles by solvent displacement. The Canadian Journal of Chemical Engineering 95, 1690–1706. doi:https://doi.org/10.1002/cjce.22867.

Flory, P., 1953. Principles of Polymer Chemistry. Ithaca: Cornell University Press.

Fox, R.O., 2003. Computational Models for Turbulent Reacting Flows. Cambridge: Cambridge University Press. doi:10.1017/CBO9780511610103.

Gartner, T.E., Jayaraman, A., 2018. Macromolecular 'size' and 'hardness' drives structure in solvent-swollen blends of linear, cyclic, and star polymers. Soft Matter 14, 411–423. doi:https://doi.org/10.1039/C7SM02199B.

Gavi, E., Marchisio, D.L., Barresi, A.A., 2007. Cfd modelling and scale-up of confined impinging jet reactors. Chemical Engineering Science 62, 2228–2241. doi:https://doi.org/10.1016/j.ces.2006.12.077.

Gradl, J., Schwarzer, H.C., Schwertfirm, F., Manhart, M., Peukert, W., 2006. Precipitation of nanoparticles in a t-mixer: coupling the particle population dynamics with hydrodynamics through direct numerical simulation. Chemical Engineering and Processing: Process Intensification 45, 908–916. doi:https://doi.org/10.1016/j.cep.2005.11.012.

Hans, M.L., Lowman, A.M., 2002. Biodegradable nanoparticles for drug delivery and targeting. Current Opinion in Solid State and Materials Science 6, 319–327. doi:https://doi.org/10.1016/S1359-0286(02)00117-1.

Hansen, C.M., 2007. Hansen Solubility Parameters: A User's Handbook (2nd edition). Boca Raton: CRC Press.

Hildebrand, J., Scott, R.L., 1950. Solubility of Nonelectrolytes (3rd edition). New York: Reinhold.

Johnson, B.K., Prud'homme, R.K., 2003a. Chemical processing and micromixing in confined impinging jets. AIChE Journal 49, 2264–2282. doi:https://doi.org/10.1002/aic.690490905.

Johnson, B.K., Prud'homme, R.K., 2003b. Flash nano-precipitation of organic actives and block copolymers using a confined impinging jets mixer. Australian Journal of Chemistry 56, 1021–1024. doi:https://doi.org/10.1071/CH03115.

888 Lavino, A.D., Banetta, L., Carbone, P., Marchisio, D.L., 2018. Ex-
889 tended charge-on-particle optimized potentials for liquid simulation ace-
890 tone model: The case of acetone–water mixtures. The Journal of Physical
891 Chemistry B 122, 5234–5241. doi:https://doi.org/10.1021/acs.jpcb.
892 8b01293.

893 Lavino, A.D., Carbone, P., Marchisio, D.L., 2020. Martini coarse-grained
894 model for poly-ε-caprolactone in acetone-water mixtures. The Canadian
895 Journal of Chemical Engineering 98, 1868–1879. doi:https://doi.org/
896 10.1002/cjce.23761.

897 Lavino, A.D., Di Pasquale, N., Carbone, P., Barresi, A.A., Marchisio, D.L.,
898 2015. Simulation of macromolecule self-assembly in solution: A multiscale
899 approach. AIP Conference Proceedings 1695, 020036. doi:https://doi.
900 org/10.1063/1.4937314.

901 Lavino, A.D., Di Pasquale, N., Carbone, P., Marchisio, D.L., 2017. A novel
902 multiscale model for the simulation of polymer flash nano-precipitation.
903 Chemical Engineering Science 171, 485–494. doi:https://doi.org/10.
904 1016/j.ces.2017.04.047.

905 Lavino, A.D., Marchisio, D.L., Vanni, M., Ferri, A., Barresi, A.A., 2019.
906 Nanoparticles production in continuous flow devices - modelling and ex-
907 perimental insights into continuous flow-based processes. Chimica Oggi -
908 Chemistry Today 37, 8–11.

909 Le Roy Boehm, A.L., Zerrouk, R., Fessi, H., 2000. Poly epsilon-caprolactone
910 nanoparticles containing a poorly soluble pesticide: formulation and sta-

bility study. Journal of Microencapsulation 17, 195–205. doi:https://doi.org/10.1080/026520400288436.

Lince, F., Marchisio, D.L., Barresi, A.A., 2008. Strategies to control the particle size distribution of poly-ε-caprolactone nanoparticles for pharmaceutical applications. Journal of Colloid and Interface Science 322, 505–515. doi:https://doi.org/10.1016/j.jcis.2008.03.033.

Lince, F., Marchisio, D.L., Barresi, A.A., 2009. Smart mixers and reactors for the production of pharmaceutical nanoparticles: Proof of concept. Chemical Engineering Research and Design 87, 543–549. doi:https://doi.org/10.1016/j.cherd.2008.11.009.

Lince, F., Marchisio, D.L., Barresi, A.A., 2011. A comparative study for nanoparticle production with passive mixers via solvent-displacement: Use of cfd models for optimization and design. Chemical Engineering and Processing: Process Intensification 50, 356–368. doi:https://doi.org/10.1016/j.cep.2011.02.015.

Liu, Y., Cheng, C., Prud'homme, R.K., Fox, R.O., 2008. Mixing in a multi-inlet vortex mixer (mivm) for flash nano-precipitation. Chemical Engineering Science 63, 2829–2842. doi:https://doi.org/10.1016/j.ces.2007.10.020.

Liu, Y., Fox, R.O., 2006. Cfd predictions for chemical processing in a confined impinging-jets reactor. AIChE Journal 52, 731–744. doi:https://doi.org/10.1002/aic.10633.

933 Marchisio, D.L., Fox, R.O., 2005. Solution of population balance equations
934 using the direct quadrature method of moments. Journal of Aerosol Science
935 36, 43–73. doi:https://doi.org/10.1016/j.jaerosci.2004.07.009.

936 Marchisio, D.L., Fox, R.O., 2013. Computational Models for Polydisperse
937 Particulate and Multiphase Flows. Cambridge: Cambridge University
938 Press.

939 Marchisio, D.L., Omegna, F., Barresi, A.A., 2009. Production of tio2
940 nanoparticles with controlled characteristics by means of a vortex reac-
941 tor. Chemical Engineering Journal 146, 456–465. doi:https://doi.org/
942 10.1016/j.cej.2008.10.031.

943 Marchisio, D.L., Omegna, F., Barresi, A.A., Bowen, P., 2008. Effect of
944 mixing and other operating parameters in sol-gel processes. Industrial &
945 Engineering Chemistry Research 47, 7202–7210. doi:https://doi.org/
946 10.1021/ie800217b.

947 Martin, T.B., Jayaraman, A., 2016. Using theory and simulations to calcu-
948 late effective interactions in polymer nanocomposites with polymer-grafted
949 nanoparticles. Macromolecules 49, 9684–9692. doi:https://doi.org/10.
950 1021/acs.macromol.6b01920.

951 Massella, D., Celasco, E., Salaün, F., Ferri, A., Barresi, A.A., 2018. Overcom-
952 ing the limits of flash nanoprecipitation: effective loading of hydrophilic
953 drug into polymeric nanoparticles with controlled structure. Polymers 10,
954 1092. doi:https://doi.org/10.3390/polym10101092.

955 Nelson, G., 2002. Application of microencapsulation in textiles. International
956 Journal of Pharmaceutics 242, 55–62. doi:https://doi.org/10.1016/
957 S0378-5173(02)00141-2.

958 Petitti, M., Vanni, M., Barresi, A.A., 2008. Controlled release of drug en-
959 capsulated as a solid core: Theoretical model and sensitivity analysis.
960 Chemical Engineering Research and Design 86, 1294–1300. doi:https:
961 //doi.org/10.1016/j.cherd.2008.05.008.

962 Prasad, R., Kumar, V., Prasad, K.S., 2014. Nanotechnology in sustain-
963 able agriculture: Present concerns and future aspects. African Journal
964 of Biotechnology 13, 705–713. doi:https://doi.org/10.5897/AJBX2013.
965 13554.

966 Rubinstein, M., Colby, R.H., 2003. Polymer Physics. Oxford: Oxford Uni-
967 versity Press.

968 Saad, W.S., 2007. Drug nanoparticle formation via flash nanoprecipitation:
969 Conjugation to encapsulate and control the release of paclitaxel. Ph.D.
970 thesis. Princeton University.

971 Saad, W.S., Prud'homme, R.K., 2016. Principles of nanoparticle formation
972 by flash nanoprecipitation. Nano Today 11, 212–227. doi:https://doi.
973 org/10.1016/j.nantod.2016.04.006.

974 Valente, I., Celasco, E., Marchisio, D.L., Barresi, A.A., 2012a. Nanopre-
975 cipitation in confined impinging jets mixers: Production, characteriza-
976 tion and scale-up of pegylated nanospheres and nanocapsules for phar-

maceutical use. Chemical Engineering Science 77, 217–227. doi:https://doi.org/10.1016/j.ces.2012.02.050.

Valente, I., Stella, B., Marchisio, D.L., Dosio, F., Barresi, A.A., 2012b. Production of pegylated nanocapsules through solvent-displacement in confined impinging jets mixers. Journal of Pharmaceutical Sciences 101, 2490–2501. doi:https://doi.org/10.1002/jps.23167.

Who, C., Jim, T., Gan, Z., Zhao, Y., Wang, S., 2000. A heterogeneous catalytic kinetics for enzymatic biodegradation of poly(ε-caprolactone) nanoparticles in aqueous solution. Polymer 41, 3593–3597. doi:https://doi.org/10.1016/S0032-3861(99)00586-8.

Wu, X., Guy, R.H., 2009. Applications of nanoparticles in topical drug delivery and in cosmetics. Journal of Drug Delivery Science and Technology 19, 371–384. doi:https://doi.org/10.1016/S1773-2247(09)50080-9.

Zelenková, T., Barresi, A.A., Fissore, D., 2015. On the use of *tert*-butanol/water cosolvent systems in production and freeze-drying of poly-ε-caprolactone nanoparticles. Journal of Pharmaceutical Sciences 104, 178–190. doi:https://doi.org/10.1002/jps.24271.

Zelenková, T., Fissore, D., Marchisio, D.L., Barresi, A.A., 2014. Size control in production and freeze-drying of poly-ε-caprolactone nanoparticles. Journal of Pharmaceutical Sciences 103, 1839–1850. doi:https://doi.org/10.1002/jps.23960.

Zelenková, T., Mora, M.J., Barresi, A.A., Granero, G.E., Fissore, D., 2018. On the production of chitosan-coated polycaprolactone nanoparticles in a

confined impinging jet reactor. Journal of Pharmaceutical Sciences 107, 1157–1166. doi:https://doi.org/10.1016/j.xphs.2017.11.020.